

Abstract

This study demonstrates that the apparent complexity of fracture in phantom-chain polymer networks is fully decoupled into two universal master curves: (i) macroscopic softening governed by the absolute stretch, and (ii) microscopic scission governed solely by the relative stretch. Using the previously proposed network mechanics model, an analytical expression has been derived to quantitatively capture the nonlinear growth of microscopic damage. Combining the softening exponent with polymer-solution scaling yields a simple novel relationship, $\sigma_{nb}/G \propto (c/c^*)^{-1/3}$, where σ_{nb} is the nominal broken strength, G is the initial shear modulus, c is the prepolymer concentration, and c^* is its overlapping threshold.

Introduction

The mechanical robustness and fracture toughness of polymer networks, such as elastomers and hydrogels, are fundamentally governed by the interplay between the macroscopic dissipation of elastic energy and the microscopic scission of polymer chains¹⁻⁶. The classical Lake-Thomas theory⁷ has long provided a foundational cornerstone, proposing that the energy required to propagate a macroscopic crack is proportional to the energy dissipated by the scission of a single polymer strand, which scales with the number of Kuhn segments in the strand^{8,9}. While the classical theory successfully captures the basic scaling for highly ideal homogeneous networks, real polymer networks invariably contain topological defects, such as dangling ends and loops,¹⁰⁻¹³ resulting from the stochastic nature of cross-linking reactions.

In real networks, the applied macroscopic stress is not uniformly distributed across all strands. Instead, topological heterogeneities induce significant non-affine deformations^{14,15}, concentrating stress on the shortest, highly stretched paths, often referred to as the weakest links^{16,17}. Consequently, macroscopic yield and fracture do not simply coincide with the simultaneous rupture of all chains. Despite extensive experimental and theoretical efforts, it remains elusive how macroscopic mechanical softening, defined as the deviation of the nominal stress from the ideal elastic prediction, quantitatively correlates with the actual fraction of microscopically broken bonds during fracture.

In a recent study¹⁸, coarse-grained molecular dynamics simulations using a phantom-chain model were conducted on end-linked star polymer networks to systematically investigate topological effects. The results demonstrated that the stretch at break, λ_b , depends on the strand molecular weight N_s with a power-law manner described as $\lambda_b \sim N_s^{0.67}$. This scaling exponent deviates from the classical single-chain Gaussian behavior $N_s^{0.5}$, although consistent with experiment¹⁹. Detailed analysis indicated that the deviation cannot be explained solely by the non-affine deformation of a single chain, but rather originates from the effective cycle rank and the network topology. However, it remained unclear what governs microscopic damage and how the phenomenon can be mathematically summarized.

In the present study, a previously proposed network mechanics model²⁰ is utilized as a framework to reconstruct the aforementioned simulation data¹⁸. Unlike the previous report²⁰, which focused on characterizing the stretch at break and topology dependence, the present study establishes two universal master curves and provides an analytical closed-form expression that unifies macroscopic softening and microscopic damage accumulation.

Simulation Methodology

The dataset analyzed in the current study was derived from the phantom chain network simulations detailed in the previous reports^{18,21–27}. The phantom chain model, which ignores excluded-volume interactions (and thus entanglements), was intentionally used to isolate the effects of network topology and connectivity on fracture behavior. Star-branched bead-spring chains were placed in a periodic boundary box with a fixed

monomer density $\rho = 8$. The total number of beads is ca. 40,000, slightly dependent on the node functionality and the arm molecular weight. The springs were Gaussian without non-linearity. To prevent the formation of primary loops, the prepolymers were colored with two different chemistries, and the reaction occurred only between different ones, mimicking tetra-PEG experiments^{28,29}. A comprehensive parameter space was explored, varying the node functionality $3 \leq f \leq 8$, arm molecular weight $2 \leq N_a \leq 20$ (where the strand molecular weight is $N_s = 2N_a + 1$), and the conversion of the end-linking reaction $0.6 \leq p \leq 0.95$. To evaluate the mechanical response, the energy-minimized networks³⁰⁻³⁵ were elongated quasi-statically by alternating between affine elongation with an infinitesimal strain and energy minimization, with volume conservation. During the elongation, bonds were removed when they exceeded a specific maximum value. The simulation continued until the network percolation was eliminated in the elongated direction. The employed quasi-static scheme avoids the effects of stretch rate and structural relaxation after each bond scission^{36,37}. Typical snapshots and stress-strain curves are shown in SI (Figs S1 and S2).

Universality of Macroscopic Softening

In the previous report¹⁸, the elongational (true) stress was measured, and the fracture strength was evaluated based on the true stress (σ_b), revealing a distinct dependence on the strand molecular weight (N_s). However, true stress is not necessarily the most appropriate parameter for evaluating the intrinsic load-bearing efficiency of the topological structure itself²⁷, and is not convenient as an experimental quantity. In this study, the fracture strength is converted to the nominal stress (σ_{nb}) in the present analysis, which is defined based on the initial, undeformed cross-sectional area. The macroscopic robustness is then re-evaluated as an effective strength ratio, σ_{nb}/G , where G is the initial shear modulus obtained from the Mooney plot of the stress-strain curve. The modulus G represents the theoretical elastic potential inherently determined by the initial cross-linking density and topology before any deformation occurs.

Since the examined networks consist of Gaussian springs, the stress-strain relation basically follows the Neo-Hookean behavior exhibiting $\sigma_n/G = (\lambda - \lambda^{-2})$ when $\lambda \ll \lambda_b$, as shown in Fig S2 (c). This relation naively suggests that $\sigma_{nb}/G \sim \lambda_b$ when λ_b is large. However, Figure 1 shows that a significant softening occurs when σ_{nb}/G is plotted against λ_b . More strikingly, when plotted based on the nominal stress criterion, the

previously observed N_s dependence completely disappears. Data from networks with entirely different arm molecular weights N_a , functionalities f , and conversion p collapse into a single master curve. Furthermore, the master curve in the primary deformation regime shows power-law behavior, $\sigma_{nb}/G \sim \lambda_b^{-1/4}$.

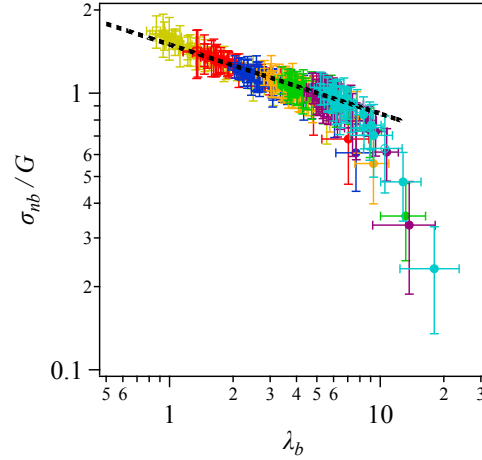


Figure 1. The macroscopic strength ratio σ_n/G plotted against the absolute stretch at break λ_b . The arm molecular weight N_a is 2 (yellow), 3 (red), 5 (blue), 8 (orange), 10 (green), 16 (violet), and 20 (cyan), respectively. Symbols indicate $f=3$ (filled circle), 4 (unfilled circle), 5 (filled triangle), 6 (unfilled triangle), 7 (filled square), and 8 (unfilled square). Error bars correspond to the standard deviations for eight different simulation runs for each condition. The data for different conversions, ranging from 0.6 to 0.95, are included. The dashed line indicates the power-law scaling $\sigma_{nb}/G \sim \lambda_b^{-1/4}$.

The physical origin of this exponent can be elucidated by invoking the scaling relations of polymer solutions^{38,39}. As reported in the previous study¹⁸, the macroscopic stretch at break scales as $\lambda_b \sim N_s^{0.67} \sim N_s^{2/3}$. (Although a rigorous bottom-up derivation of this scaling remains an open theoretical challenge, the relation has been empirically observed in the simulation¹⁸ and experiment¹⁹.) Simultaneously, under a constant monomer density, the normalized prepolymer concentration relative to the overlap concentration scales as $c/c^* \sim N_s^{1/2}$. These scaling relations lead to $c/c^* \sim \lambda_b^{3/4}$. The exponent 3/4 originates from the geometric dilution of load-bearing paths under affine volume conservation, combined with the increase of c^* at larger N_s . Therefore, the effective number of parallel load-bearing paths decreases as $\lambda_b^{-3/4}$, naturally producing the observed softening $\sigma_{nb}/G \sim \lambda_b^{-1/4}$.

Consequently, the observed macroscopic softening can be transformed into the following scaling formula.

$$\frac{\sigma_{nb}}{G} \sim \left(\frac{c}{c^*}\right)^{-\frac{1}{3}} \quad (1)$$

It is crucial to note the physical meaning of c/c^* in the context of phantom chain networks. Although phantom chains lack excluded-volume and osmotic interactions, c/c^* during the cross-linking reaction serves as a purely geometric parameter that strictly dictates the degree of topological redundancy. A higher c/c^* implies that a larger number of chains share the same pervaded volume, inevitably resulting in a more complex network topology with highly redundant load-bearing paths. Indeed, as reported previously²⁶, phantom networks created with larger c exhibit better rupture resistance.

To directly validate this relationship, σ_{nb}/G is plotted against c/c^* in Figure 2. Remarkably, despite including data with varying conversion, the vast majority of the points collapse onto the predicted $-1/3$ power-law master curve in the primary region. It should be noted that a downward deviation from this scaling is observed for a specific subset of data, which corresponds to networks with the smallest functionality ($f = 3$) at the lowest conversion ($p = 0.6$). As explicitly categorized out of the theoretical scope in the previously proposed framework²⁰, such highly incomplete networks are situated in the immediate vicinity of the gelation threshold. In this extreme regime, macroscopic percolation is barely sustained by a highly fragile topology, causing the macroscopic load-bearing efficiency to deteriorate more severely than the mean-field c/c^* scaling prediction. The macroscopic strength σ_{nb}/G exhibits another rapid decay deviating from this power-law at extreme elongations ($\lambda_b \gtrsim 7$). As discussed later, the deviation reflects a structural transition of the load-bearing paths.

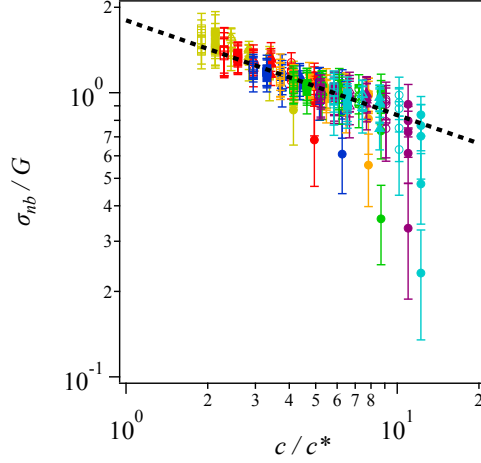


Figure 2. The macroscopic strength ratio σ_n/G plotted against the normalized prepolymer concentration c/c^* . The arm molecular weight N_a is 2 (yellow), 3 (red), 5 (blue), 8 (orange), 10 (green), 16 (violet), and 20 (cyan), respectively. Symbols indicate $f=3$ (filled circle), 4 (unfilled circle), 5 (filled triangle), 6 (unfilled triangle), 7 (filled square), and 8 (unfilled square). Error bars correspond to the standard deviations for eight different simulation runs for each condition. The data for different conversions, ranging from 0.6 to 0.95, are included. The dashed line indicates the power-law scaling $\sigma_{nb}/G \sim (c/c^*)^{-1/3}$.

Topological Scaling of Microscopic Damage

Since macroscopic softening is due to the microscopic bond scission, let us turn our attention to the fraction of strands broken in the entire system, ϕ_b . A naive plot of ϕ_b versus λ_b exhibits a severe splitting of the data, dependent on the strand length N_s (see Fig S3), implying that local bond breaking does not share the same scaling as the global stress behavior. To resolve the parameter dependency, a normalization scheme that accounts for both the specific topology and the spatial scale of the fracture zone is required. First, to account for differences in f and p , ϕ_b is multiplied by the effective number of strands connected per network node, expressed as $(\xi + 1)$, where ξ is the cycle rank per network node. Second, based on the Lake-Thomas conceptual framework^{7,40}, the thickness of the local damage zone is assumed to be proportional to the inherent critical stretch of the single strand, λ_{b1} . (This parameter has been introduced in the previous study²⁰ to characterize the maximum local stretch.) Consequently, a dimensionless damage parameter can be written as $\phi_b(\xi + 1)/\lambda_{b1}$. In Figure 3 (a), this parameter is plotted against the relative deformation λ_b/λ_{b1} . The result reveals that all previously scattered data collapse into a single master curve. Besides, Figure 3 (b) indicates that the damage parameter is proportional to the cycle rank when ξ is sufficiently large.

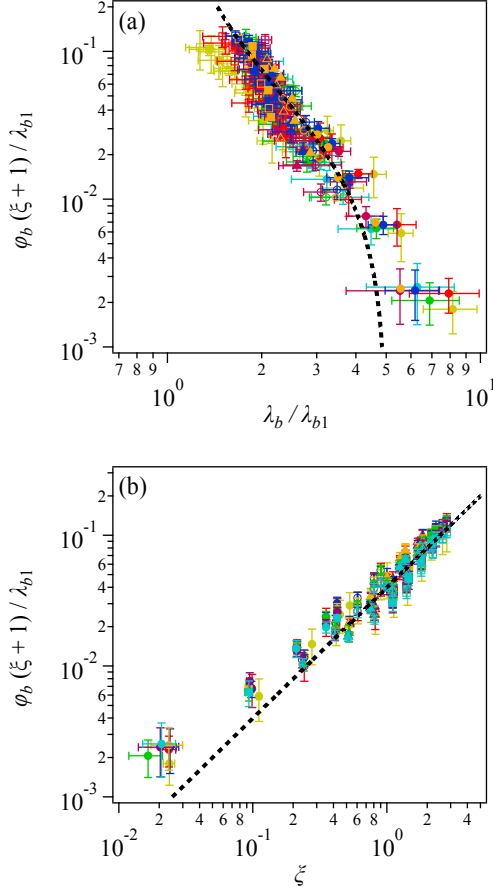


Figure 3. Dimensionless microscopic damage fraction $\phi_b(\xi + 1)/\lambda_{b1}$ plotted against the relative deformation λ_b/λ_{b1} (a) and the cycle rank ξ (b). The arm molecular weight N_a is 2 (yellow), 3 (red), 5 (blue), 8 (orange), 10 (green), 16 (violet), and 20 (cyan), respectively. Symbols indicate $f = 3$ (filled circle), 4 (unfilled circle), 5 (filled triangle), 6 (unfilled triangle), 7 (filled square), and 8 (unfilled square). Error bars correspond to the standard deviations for eight different simulation runs for each condition. The data for different conversions, ranging from 0.6 to 0.95, are included. The dashed curve in panel (a) shows eq (3), and the line in panel (b) indicates a linear relation.

Unification via Network Mechanics Model

Counterintuitively, the absolute deformation-governed macroscopic softening and the relative deformation-governed microscopic scission appear decoupled. The fundamental reason for this decoupling lies in the distinct physical origins of the macroscopic and microscopic responses. Macroscopic softening is a global geometric phenomenon driven by the non-affine spatial rearrangement and the dilution of effective load-bearing paths during large deformation. Consequently, the softening is intrinsically governed by the absolute macroscopic stretch of the entire system (λ_b) and the relative congestion of chains (c/c^*). Conversely, microscopic bond scission is a strictly local event triggered when the bond length of a specific strand exceeds

its intrinsic limit. Thus, the scission is dictated solely by how much the individual strand is stretched relative to its own extensibility limit (λ_b/λ_{b1}).

While the two phenomena are decoupled by their different governing length scales, they can be bridged using the framework of the previously reported network mechanics model²⁰, which proposes a macroscopic fracture criterion by relating the macroscopic stretch (λ_b), the local intrinsic limit of a single strand (λ_{b1}), and the cycle rank (ξ).

$$\lambda_b = \lambda_{b1} \left(\frac{2\xi + 5}{2\xi + 1} \right) \quad (2)$$

Here, ξ is the difference between the numbers of effective strands and nodes per branch point, and thus, a global ensemble-averaged topological parameter. The central role of network cycles and redundant paths in determining the elastic response was already emphasized in the classical James–Guth theory^{41,42} of rubber elasticity, which first established that the network topology determines its collective deformation modes. Figure 4 demonstrates that when the relative macroscopic stretch λ_b/λ_{b1} is plotted against the cycle rank ξ , the scattered data points are excellently described by the theoretical curve in the primary region.

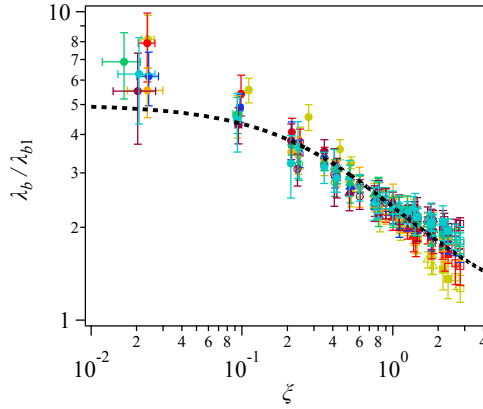


Figure 4. The relative macroscopic stretch at break λ_b/λ_{b1} plotted against the cycle rank ξ . The arm molecular weight N_a is 2 (yellow), 3 (red), 5 (blue), 8 (orange), 10 (green), 16 (violet), and 20 (cyan), respectively. Symbols indicate $f=3$ (filled circle), 4 (unfilled circle), 5 (filled triangle), 6 (unfilled triangle), 7 (filled square), and 8 (unfilled square). Error bars correspond to the standard deviations for eight different simulation runs for each condition. The data for different conversions, ranging from 0.6 to 0.95, are included. The dashed curve indicates eq (2).

Meanwhile, the normalized dimensionless damage quantity $\phi_b(\xi + 1)/\lambda_{b1}$ appears proportional to the cycle rank ξ over a wide parameter range, as shown in Figure 3 (b). The proportionality signifies a profound yet physically intuitive topological requirement: the total number of microscopic bond scissions required to induce macroscopic network failure is directly proportional to the total number of redundant, load-bearing cycle ranks (backup paths) initially possessed by the system. In other words, a network capacity to absorb microscopic damage scales linearly with its topological redundancy, naturally leading to this exact proportional relationship.

The results in Figs 3(b) and 4 yield an analytical function that describes the microscopic damage accumulation as follows.

$$\frac{\phi_b(\xi + 1)}{\lambda_{b1}} \sim \frac{5 - (\lambda_b/\lambda_{b1})}{2(\lambda_b/\lambda_{b1} - 1)} \quad (3)$$

Equation 3 follows uniquely from substituting eq (2) into the linear damage–cycle-rank relation in Fig. 3(b), without any empirical fitting. The dashed curve in Figure 3 (a) demonstrates that eq (3) reproduces the data within the computational error bars. This result implies that the macroscopic fracture criterion successfully unifies the decoupled global softening and local bond scission into a single analytical formulation.

Structural Transition of the Weakest Link near the Percolation Limit

While eq (3) successfully describes the multiscale fracture behaviors, noticeable deviations are observed in both macroscopic and microscopic master curves at the extreme limits. Specifically, at the low- ξ range, the dimensionless damage deviates from the proportionality (Figure 3(b)), and similarly, the macroscopic stretch deviates from eq (2) (Figure 4). These deviations correspond exactly to the rapid stress drop observed in the macroscopic softening curve at extreme stretches in $\lambda_b \gtrsim 7$ (Figure 1). As previously discussed²⁰, these deviations are neither mere statistical noise nor simulation artifacts, but reflect a fundamental structural transition in the fracture mechanism. In well-connected networks with relatively large ξ , the weakest link that triggers macroscopic failure is localized to a small number of individual strands. In contrast, as the network approaches the percolation threshold ($\xi \rightarrow 0$), the macroscopic load is sustained by sparse paths.

Under such conditions, in particular near the gel point, the load-bearing backbone becomes a sparse tree-like structure where long serial sequences of strands naturally emerge, increasing the effective weakest-link length. Because the effective length of the critical load-bearing path changes, the fracture criteria deviate from the simple scaling based on the single-strand limit λ_{b1} . The concurrent deviations observed across Figures 1, 3, and 4 indicate that the network topology loses redundancy.

Conclusions

The present study demonstrates that the fracture of polymer networks, which traditionally exhibits highly complex phenomenological dependencies on molecular weight, functionality, and defects, can be physically decoupled into two distinct scaling laws. The microscopic structural collapse (bond scission) is governed by the relative deformation at the local scale, which is mathematically unified by the effective cycle rank ξ and the weakest-link spatial scale λ_{b1} , utilizing the network mechanics model²⁰. The successful reproduction of the microscopic scission master curve as an analytical solution implies that polymer fracture is governed by network topology.

More importantly for experimental applications, the present study proposes two highly accessible, universal scaling rules in macroscopic fracture mechanics. First, the macroscopic effective strength ratio collapses into a universal master curve when plotted against the absolute stretch at break as $\sigma_{nb}/G \sim \lambda_b^{-1/4}$. Second, by connecting the power-law softening observed in the primary deformation regime with the scaling of the overlap concentration, an interesting scaling relationship is obtained as $\sigma_{nb}/G \sim (c/c^*)^{-1/3}$. These scaling relations are entirely independent of the strand molecular weight, node functionality, and conversion. These findings suggest that the macroscopic fracture robustness of elastomers and hydrogels is governed not by the specific local extensibility of individual strands, but by the global geometric deformation and the topological complexity of the initial network.

Note, however, that the results obtained are for phantom Gaussian chain networks generated from monodisperse star prepolymers, which miss important physics in real networks, such as excluded-volume interactions, crystallization, osmotic forces, finite extensibility, and strand-length distributions. Because

reported datasets on the rupture characteristics of polymer networks are rather rare, examining the proposed relations against experimental and simulation data for these aspects is ongoing, and the results will be published elsewhere.

Acknowledgement

This study was partly supported by the Hibi Foundation and the Eno Science Foundation.

References

- (1) Gong, J. P. Why Are Double Network Hydrogels so Tough? *Soft Matter* **2010**, *6* (12), 2583. <https://doi.org/10.1039/b924290b>.
- (2) Zhao, X. Multi-Scale Multi-Mechanism Design of Tough Hydrogels: Building Dissipation into Stretchy Networks. *Soft Matter* **2014**, *10* (5), 672–687. <https://doi.org/10.1039/c3sm52272e>.
- (3) Creton, C.; Ciccotti, M. Fracture and Adhesion of Soft Materials: A Review. *Reports on Progress in Physics*. Institute of Physics Publishing March 23, 2016. <https://doi.org/10.1088/0034-4885/79/4/046601>.
- (4) Creton, C. 50th Anniversary Perspective: Networks and Gels: Soft but Dynamic and Tough. *Macromolecules* **2017**, *50* (21), 8297–8316. <https://doi.org/10.1021/acs.macromol.7b01698>.
- (5) Sakai, Takamasa. *Physics of Polymer Gels*; Sakai, T., Ed.; Wiley, 2020. <https://doi.org/10.1002/9783527346547>.
- (6) Lake, J.; Thomas, A. G. The Strength of Highly Elastic Materials. *Proc. R. Soc. Lond. A Math. Phys. Sci.* **1967**, *300* (1460), 108–119. <https://doi.org/10.1098/rspa.1967.0160>.
- (7) Kuhn, W. Dependence of the Average Transversal on the Longitudinal Dimensions of Statistical Coils Formed by Chain Molecules. *Journal of Polymer Science* **1946**, *1* (5), 380–388. <https://doi.org/10.1002/pol.1946.120010505>.
- (8) Obukhov, S. P.; Rubinstein, M.; Colby, R. H. *Network Modulus and Superelasticity*; 1994; Vol. 27. <https://pubs.acs.org/sharingguidelines>.
- (9) Zhou, H.; Woo, J.; Cok, A. M.; Wang, M.; Olsen, B. D.; Johnson, J. A. Counting Primary Loops in Polymer Gels. *Proc. Natl. Acad. Sci. U. S. A.* **2012**, *109* (47), 19119–19124. <https://doi.org/10.1073/pnas.1213169109>.

- (10) Zhong, M.; Wang, R.; Kawamoto, K.; Olsen, B. D.; Johnson, J. A. Quantifying the Impact of Molecular Defects on Polymer Network Elasticity. *Science (1979)*. **2016**, *353* (6305), 1264–1268. <https://doi.org/10.1126/science.aag0184>.
- (11) Barney, C. W.; Ye, Z.; Sacligil, I.; McLeod, K. R.; Zhang, H.; Tew, G. N.; Riggelman, R. A.; Crosby, A. J. Fracture of Model End-Linked Networks. *Proceedings of the National Academy of Sciences* **2022**, *119* (7), 2–7. <https://doi.org/10.1073/pnas.2112389119>.
- (12) Danielsen, S. P. O.; Beech, H. K.; Wang, S.; El-Zaatari, B. M.; Wang, X.; Sapir, L.; Ouchi, T.; Wang, Z.; Johnson, P. N.; Hu, Y.; Lundberg, D. J.; Stoychev, G.; Craig, S. L.; Johnson, J. A.; Kalow, J. A.; Olsen, B. D.; Rubinstein, M. Molecular Characterization of Polymer Networks. *Chem. Rev.* **2021**, *121* (8), 5042–5092. <https://doi.org/10.1021/acs.chemrev.0c01304>.
- (13) Stevens, M. J. Manipulating Connectivity to Control Fracture in Network Polymer Adhesives. *Macromolecules* **2001**, *34* (5), 1411–1415. <https://doi.org/10.1021/ma0009505>.
- (14) Yu, Z.; Jackson, N. E. Shortest Paths Govern Bond Rupture in Thermoset Networks. *Macromolecules* **2025**, *58* (3), 1728–1736. <https://doi.org/10.1021/acs.macromol.4c02438>.
- (15) Masubuchi, Y. Phantom Chain Simulations for the Fracture of Star Polymer Networks on the Effect of Arm Molecular Weight. *Macromolecules* **2025**, *58* (12), 6399–6405. <https://doi.org/10.1021/acs.macromol.5c00475>.
- (16) Akagi, Y.; Katashima, T.; Sakurai, H.; Chung, U. Il; Sakai, T. Ultimate Elongation of Polymer Gels with Controlled Network Structure. *RSC Adv.* **2013**, *3* (32), 13251–13258. <https://doi.org/10.1039/c3ra41580e>.
- (17) Masubuchi, Y. A Toy Model for the Cycle Rank Dependence of Stretch at Break in Phantom Chain Network Simulations. **2026**.
- (18) Masubuchi, Y.; Doi, Y.; Ishida, T.; Sakumichi, N.; Sakai, T.; Mayumi, K.; Uneyama, T. Phantom Chain Simulations for the Fracture of Energy-Minimized Tetra- and Tri-Branched Networks. *Macromolecules* **2023**, *56* (5), 2217–2223. <https://doi.org/10.1021/acs.macromol.3c00047>.
- (19) Masubuchi, Y.; Doi, Y.; Ishida, T.; Sakumichi, N.; Sakai, T.; Mayumi, K.; Satoh, K.; Uneyama, T. Phantom-Chain Simulations for the Effect of Node Functionality on the Fracture of Star-Polymer Networks. *Macromolecules* **2023**, *56* (23), 9359–9367. <https://doi.org/10.1021/acs.macromol.3c01291>.

- (20) Masubuchi, Y. Phantom Chain Simulations for the Effect of Stoichiometry on the Fracture of Star-Polymer Networks. *Nihon Reoroji Gakkaishi* **2024**, *52* (1), 21–26. <https://doi.org/10.1678/rheology.52.21>.
- (21) Masubuchi, Y. Phantom Chain Simulations for Fracture of End-Linking Networks. *Polymer (Guildf)*. **2024**, *297*, 126880. <https://doi.org/10.1016/j.polymer.2024.126880>.
- (22) Masubuchi, Y. Phantom Chain Simulations for Fracture of Polymer Networks Created from Star Polymer Mixtures of Different Functionalities. *Polym. J.* **2024**, *56* (3), 163–171. <https://doi.org/10.1038/s41428-023-00862-w>.
- (23) Masubuchi, Y.; Ishida, T.; Koide, Y.; Uneyama, T. Phantom Chain Simulations for the Fracture of Star Polymer Networks with Various Strand Densities. *Soft Matter* **2024**, *20*, 7103–7110. <https://doi.org/10.1039/D4SM00726C>.
- (24) Masubuchi, Y.; Ishida, T.; Koide, Y.; Uneyama, T. Influence of Stretching Boundary Conditions on Fracture in Phantom Star Polymer Networks: From Volume to Cross-Sectional Area Conservation. **2025**. <https://doi.org/10.48550/arXiv.2509.01844>.
- (25) Sakai, T.; Matsunaga, T.; Yamamoto, Y.; Ito, C.; Yoshida, R.; Suzuki, S.; Sasaki, N.; Shibayama, M.; Chung, U. Design and Fabrication of a High-Strength Hydrogel with Ideally Homogeneous Network Structure from Tetrahedron-like Macromonomers. *Macromolecules* **2008**, *41* (14), 5379–5384. <https://doi.org/10.1021/ma800476x>.
- (26) Sakai, T. Gelation Mechanism and Mechanical Properties of Tetra-PEG Gel. *React. Funct. Polym.* **2013**, *73* (7), 898–903. <https://doi.org/10.1016/j.reactfunctpolym.2013.03.015>.
- (27) Nishi, K.; Noguchi, H.; Sakai, T.; Shibayama, M. Rubber Elasticity for Percolation Network Consisting of Gaussian Chains. *J. Chem. Phys.* **2015**, *143* (18), 184905. <https://doi.org/10.1063/1.4935395>.
- (28) Nishi, K.; Chijiishi, M.; Katsumoto, Y.; Nakao, T.; Fujii, K.; Chung, U.; Noguchi, H.; Sakai, T.; Shibayama, M. Rubber Elasticity for Incomplete Polymer Networks. *J. Chem. Phys.* **2012**, *137* (22), 224903. <https://doi.org/10.1063/1.4769829>.
- (29) Lang, M. On the Elasticity of Polymer Model Networks Containing Finite Loops. *Macromolecules* **2019**, *52* (16), 6266–6273. <https://doi.org/10.1021/acs.macromol.9b00996>.

- (30) Arora, A.; Lin, T.-S.; Beech, H. K.; Mochigase, H.; Wang, R.; Olsen, B. D. Fracture of Polymer Networks Containing Topological Defects. *Macromolecules* **2020**, *53* (17), 7346–7355. <https://doi.org/10.1021/acs.macromol.0c01038>.
- (31) Arora, A.; Lin, T. S.; Olsen, B. D. Coarse-Grained Simulations for Fracture of Polymer Networks: Stress Versus Topological Inhomogeneities. *Macromolecules* **2022**, *55* (1), 4–14. <https://doi.org/10.1021/acs.macromol.1c01689>.
- (32) Arora, A. Effect of Spatial Heterogeneity on the Elasticity and Fracture of Polymer Networks. *Macromolecules* **2025**, *58* (2), 1143–1155. <https://doi.org/10.1021/acs.macromol.4c01533>.
- (33) Masubuchi, Y.; Yamazaki, R.; Doi, Y.; Uneyama, T.; Sakumichi, N.; Sakai, T. Brownian Simulations for Tetra-Gel-Type Phantom Networks Composed of Prepolymers with Bidisperse Arm Length. *Soft Matter* **2022**, *18*, 4715–4724. <https://doi.org/10.1039/d2sm00488g>.
- (34) Masubuchi, Y.; Koide, Y.; Ishida, T.; Uneyama, T. Brownian Simulations for Fracture of Star Polymer Phantom Networks. *Polym. J.* **2025**, *57* (4), 483–489. <https://doi.org/10.1038/s41428-024-00992-9>.
- (35) de Gennes, P. G. *Scaling Concepts in Polymer Physics*; Cornell University Press: Ithaca, 1979.
- (36) Rubinstein, M.; Colby, R. H. *Polymer Physics*; Oxford University Press: Oxford, 2003. <https://doi.org/10.1093/oso/9780198520597.001.0001>.
- (37) Wang, S.; Panyukov, S.; Rubinstein, M.; Craig, S. L. Quantitative Adjustment to the Molecular Energy Parameter in the Lake-Thomas Theory of Polymer Fracture Energy. *Macromolecules* **2019**, *52* (7), 2772–2777. <https://doi.org/10.1021/acs.macromol.8b02341>.

Supporting Information for

Universal Scaling of Macroscopic Softening and Microscopic Scission in Phantom Chain Networks

Yuichi Masubuchi*

Department of Materials Physics, Nagoya University, Nagoya 4648603, Japan

E-mail: mas@mp.pse.nagoya-u.ac.jp

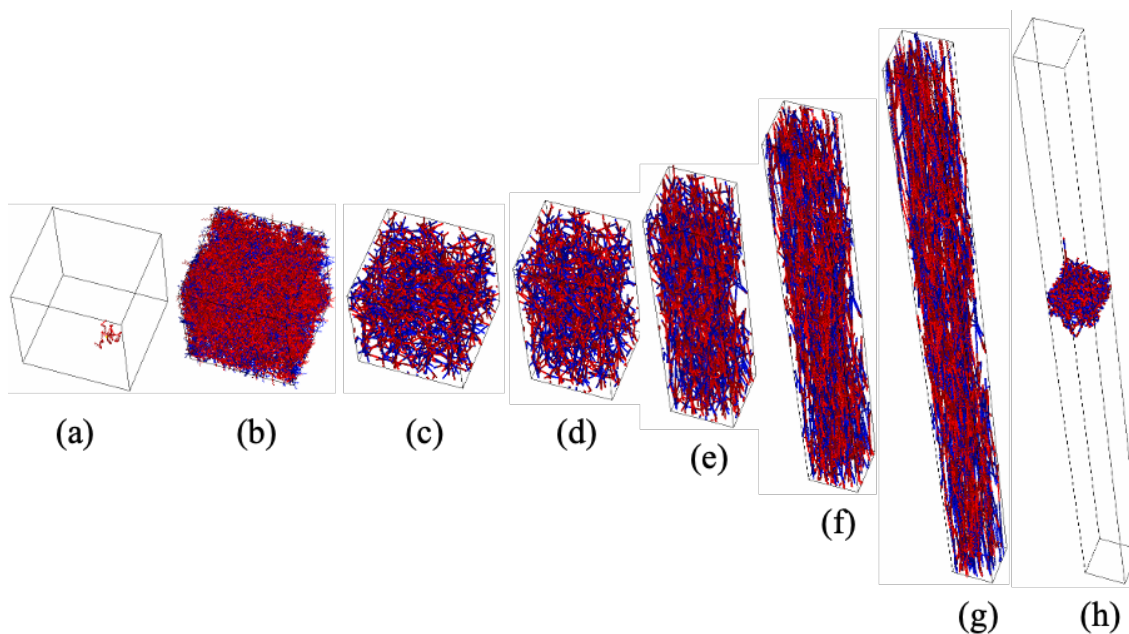


Figure S1. Typical snapshots during the simulation with $f = 4$ and $N_a = 8$ for a single prepolymer (a), the end-linked network containing 1050 prepolymers with the conversion $p = 0.9$ (b), the energy-minimized structure (c), the elongated structures at $\lambda = 1.6, 2.7, 4.5,$ and 6.7 (d)-(g), and the broken structure at $\lambda = 6.9$ (h), respectively. Red and blue colors indicate different chemistries for the end-linking reaction. The simulations were performed with nondimensionalized quantities, and the units of length, energy, and time were the average bond length under equilibrium (before energy minimization), thermal energy, and the bead diffusion time. For the Brownian dynamics, a second-order integration scheme was employed, with the step size of $\Delta t = 0.01$. The parameters for the end-linking reaction were the critical distance of $r_r = 1$ and the reaction probability of $p_r = 0.1$. The energy minimization scheme was the Broyden-Fletcher-Goldfarb-Sanno method with the bead displacement parameter of $\Delta r = 0.01$, and the energy conversion parameter of $\Delta u = 10^{-4}$. The system volume was conserved under elongation. The magnitude of elongation at the stepwise stretch was $\Delta \varepsilon = 0.01$. The bond scission parameter b_c was fixed at $\sqrt{1.5}$. For statistics, eight independent simulation runs were performed for each set of parameters.

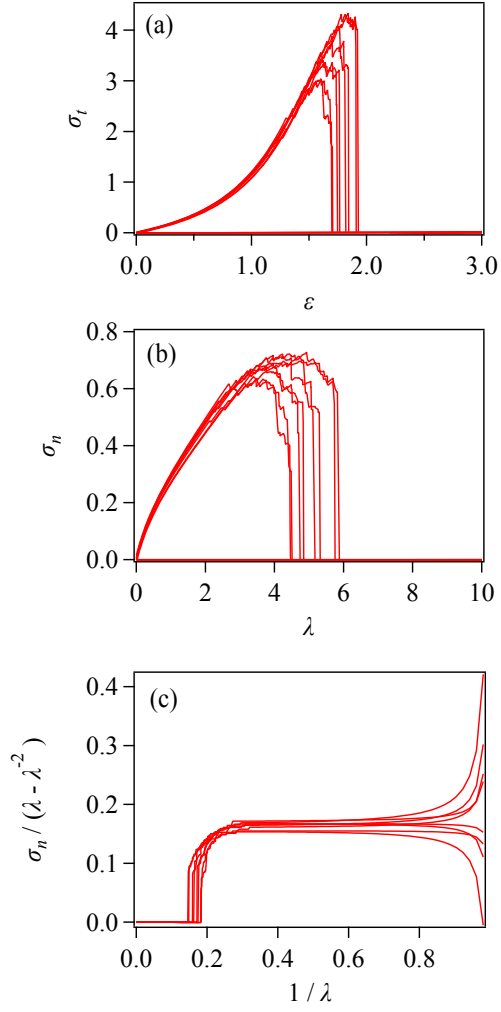


Figure S2. Stress-strain curves for the networks with $f = 4$, $N_a = 8$, and $p = 0.9$ in true stress versus true strain (a), nominal stress versus stretch (b), and Mooney plot. Each curve indicate independent simulation run. The stretch and stress at break, λ_b and σ_{nb} in the main text, were defined from the peak of the curve in panel (b). The shear modulus G was determined from the plateau in panel (c).

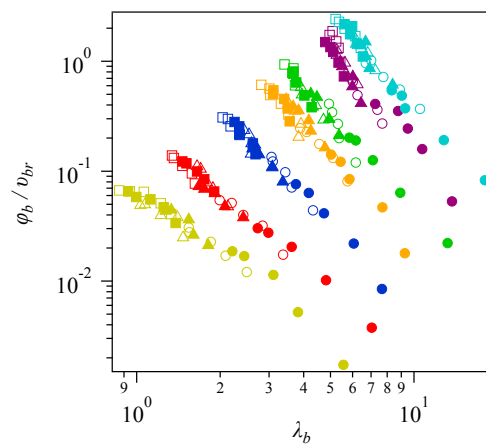


Figure S3. The broken bond fraction ϕ_b normalized by the node number density ν_{br} plotted against the absolute stretch at break λ_b . The arm molecular weight N_a is 2 (yellow), 3 (red), 5 (blue), 8 (orange), 10 (green), 16 (violet), and 20 (cyan), respectively. Symbols indicate $f=3$ (filled circle), 4 (unfilled circle), 5 (filled triangle), 6 (unfilled triangle), 7 (filled square), and 8 (unfilled square). The data for different conversions, ranging from 0.6 to 0.95, are included.